extrapolates to zero splitting at $B = 0$ (*21*), in contradiction to the data (SOM S7). Integer values of $S \geq 2$ can be ruled out on the basis of the temperature scaling described above and because previous studies of sixfold coordinated Co complexes have found almost exclusively $S \leq 3/2$, with exceptions only for fluoride ligands (*1*, *2*). We conclude that only $S = 1$ can explain the measurements, and from this we identify the charge state of the metal center to be Co^{1+} (SOM S8).

In coordination chemistry, the existence of zero-field splittings induced by molecular distortion is well established, but the ability we demonstrate to continuously distort an individual molecule while simultaneously measuring its zero-field splitting opens the possibility for dramatically more detailed and precise comparisons with theory. For correlated-electron physics, our results demonstrate that single-molecule electrical devices can provide well-controlled model systems for studying $S \geq 1$ underscreened Kondo effects not previously realizable in experiment. Our work further demonstrates that mechanical control can be a realistic strategy for manipulating molecular spin states to supplement or replace the use of magnetic fields in proposed applications such as quantum manipulation or information storage (*27*, *28*).

References and Notes

1. A. Abragam, B. Bleaney, *Electron Paramagnetic Resonance of Transition Ions* (Dover, New York, 1986).
2. R. Boca, *Coord. Chem. Rev.* **248**, 757 (2004).
3. N. Agraït, A. L. Yeyati, J. M. van Ruitenbeek, *Phys. Rep.* **377**, 81 (2003).
4. F. Mallet *et al.*, *Phys. Rev. Lett.* **97**, 226804 (2006).
5. P. Nozières, A. Blandin, *J. Phys. (Paris)* **41**, 193 (1980).
6. A. Posazhennikova, P. Coleman, *Phys. Rev. Lett.* **94**, 036802 (2005).
7. P. Mehta, N. Andrei, P. Coleman, L. Borda, G. Zarand, *Phys. Rev. B* **72**, 014430 (2005).
8. J. Park *et al.*, *Nature* **417**, 722 (2002).
9. M. Grobis, I. G. Rau, R. M. Potok, D. Goldhaber-Gordon, in *Handbook of Magnetism and Advanced Magnetic Materials*, H. Kronmüller, S. S. P. Parkin, Eds. (Wiley, Hoboken, NJ, 2007).
10. C. Romeike, M. R. Wegewijs, W. Hofstetter, H. Schoeller, *Phys. Rev. Lett.* **97**, 206601 (2006).
11. W. Liang, M. P. Shores, M. Bockrath, J. R. Long, H. Park, *Nature* **417**, 725 (2002).
12. A. Zhao *et al.*, *Science* **309**, 1542 (2005).
13. L. H. Yu *et al.*, *Phys. Rev. Lett.* **93**, 266802 (2004).
14. X. H. Qiu, G. V. Nazin, W. Ho, *Phys. Rev. Lett.* **92**, 206102 (2004).
15. D.-H. Chae *et al.*, *Nano Lett.* **6**, 165 (2006).
16. H. B. Heersche *et al.*, *Phys. Rev. Lett.* **96**, 206801 (2006).
17. M.-H. Jo *et al.*, *Nano Lett.* **6**, 2014 (2006).
18. H. Park, A. K. L. Lim, A. P. Alivisatos, J. Park, P. L. McEuen, *Appl. Phys. Lett.* **75**, 301 (1999).
19. Materials and methods are available as supporting material on *Science* Online.
20. J. J. Parks *et al.*, *Phys. Rev. Lett.* **99**, 026601 (2007).
21. A. F. Otte *et al.*, *Nat. Phys.* **4**, 847 (2008).
22. M. Pustilnik, L. I. Glazman, *Phys. Rev. Lett.* **87**, 216601 (2001).
23. T. A. Costi, A. C. Hewson, V. Zlatic, *J. Phys. Cond. Matter* **6**, 2519 (1994).
24. D. Goldhaber-Gordon *et al.*, *Phys. Rev. Lett.* **81**, 5225 (1998).
25. J. J. Parks, thesis, Cornell University, Ithaca, NY (2009).
26. N. Roch, S. Florens, T. A. Costi, W. Wernsdorfer, F. Balestro, *Phys. Rev. Lett.* **103**, 197202 (2009).
27. G. Christou, D. Gatteschi, D. N. Hendrickson, R. Sessoli, *MRS Bull.* **25**, 66 (November 2000).
28. L. Bogani, W. Wernsdorfer, *Nat. Mater.* **7**, 179 (2008).

29. We thank I. Cohen, M. Grobis, G. Hutchison, and P. McEuen for discussions and K. Bolotin, J. Grose, F. Kuemmeth, and E. Tam for technical help. Research at Cornell was supported by the NSF through the Cornell Center for Materials Research, DMR-0605742, CHE-0403806, and use of the Cornell Nanofabrication Facility/National Nanotechnology Infrastructure Network. T.A.C. acknowledges supercomputer support by the John von Neumann Institute for Computing (Jülich). P.S.C., A.A.A., and C.A.B. were supported by Proyectos de Investigación Plurianuales 11220080101821 of CONICET.

Supporting Online Material

www.sciencemag.org/cgi/content/full/328/5984/1370/DC1
Materials and Methods
SOM Text
Figs. S1 to S8
Table S1
References

11 January 2010; accepted 29 April 2010
10.1126/science.1186874

Nanoscale Tunable Reduction of Graphene Oxide for Graphene Electronics

Zhongqing Wei,[1]* Debin Wang,[2]* Suenne Kim,[2] Soo-Young Kim,[3,4] Yike Hu,[2] Michael K. Yakes,[1] Arnaldo R. Laracuente,[1] Zhenting Dai,[5] Seth R. Marder,[3] Claire Berger,[2,6] William P. King,[5] Walter A. de Heer,[2] Paul E. Sheehan,[1]† Elisa Riedo[2]†

The reduced form of graphene oxide (GO) is an attractive alternative to graphene for producing large-scale flexible conductors and for creating devices that require an electronic gap. We report on a means to tune the topographical and electrical properties of reduced GO (rGO) with nanoscopic resolution by local thermal reduction of GO with a heated atomic force microscope tip. The rGO regions are up to four orders of magnitude more conductive than pristine GO. No sign of tip wear or sample tearing was observed. Variably conductive nanoribbons with dimensions down to 12 nanometers could be produced in oxidized epitaxial graphene films in a single step that is clean, rapid, and reliable.

Graphene's high electronic mobility (*1*) has been harnessed in devices such as transistors operating at gigahertz frequency (*2*); however, the zero band gap of graphene leads to high leakage currents in many applications. Another interesting material for a range of applications is graphene oxide (GO) (*3*, *4*), which exhibits a transport gap greater than 0.5 eV at room temperature and becomes a semiconductor or semimetal as it is reduced back toward graphene (*5*, *6*). Reduced GO (rGO) resembles graphene but with some residual oxygen and structural defects, yielding a conductivity that is comparable to that of doped conductive polymers (*7*) and 33,000 times higher than that of doped hydrogenated amorphous Si (*8*). Reduced GO can also be used in highly sensitive gas sensors (*9*) and mechanical resonators with figures of merit surpassing those of graphene resonators (*10*).

We present a tip-based thermochemical nanolithography method to control the extent of reduction of GO and pattern nanoscale regions of rGO within a GO sheet at speeds of several μm/s. The relative increase in conductivity is as high as four orders of magnitude. GO was converted to rGO with a 100% yield in dozens of structures patterned on random locations in the GO film. Reduced GO patterns range from ribbons 12 nm in width (full width at half maximum, FWHM) up to 20 μm. No sign of tip wear or sample tearing was observed, indicating that the "carbon skeleton" is continuous across the GO/rGO junction. Thermochemical nanolithography (TCNL) with heated probe tips can localize thermally induced chemical reactions on a surface (*11*–*14*) or deposit material (*15*–*17*). Similar heated tips have also been used to mechanically modify a polymer film (*18*). We performed TCNL by using a heated atomic force microscope (AFM) probe tip to reduce selected regions of both single layers of isolated GO and large-area GO films formed by on-chip oxidation of epitaxial graphene (GO_{epi}) grown on SiC.

Exposure of GO to strong reducing agents like hydrazine results in an increased electrical conductivity by three to four orders of magnitude (*19*). Thermal reduction of GO occurs already at moderate temperature (100° to 250°C) and enables tuning the gap in graphene oxide (*6*), as demonstrated in its current-voltage (*I*-*V*) characteristics. Recent studies have shown that annealing

[1]Chemistry Division, U.S. Naval Research Laboratory, Code 6177, Washington, DC 20375, USA. [2]School of Physics, Georgia Institute of Technology, Atlanta, GA 30332, USA. [3]School of Chemistry and Biochemistry, Georgia Institute of Technology, Atlanta, GA 30332, USA. [4]School of Chemical Engineering and Materials Science, Chung Ang University, Seoul 156-756, Republic of Korea. [5]Department of Mechanical Science and Engineering, University of Illinois Urbana-Champaign, Urbana, IL 61801, USA. [6]CNRS-Institut Néel, BP166, 38042 Grenoble Cedex 9, France.

*These authors contributed equally to this work.
†To whom correspondence should be addressed. E-mail: paul.sheehan@nrl.navy.mil (P.E.S.); elisa.riedo@physics.gatech.edu (E.R.)

GO at 450°C or above is equivalent to chemical reduction via hydrazine monohydrate at 80°C followed by heating at 200°C (*20*). We verified TCNL reduction of GO by friction force microscopy (FFM), conductive AFM (CAFM), Raman spectroscopy, Kelvin probe force microscopy (KPFM), and ultrahigh-vacuum (UHV) electronic transport measurements using a two- and four-point probe scanning tunneling microscope (STM) [see details in the supporting online material (SOM) (*21*)].

Arbitrary rGO features such as a cross (Fig. 1) or squares (Fig. 2) are reliably obtained by scanning the heated AFM tip over isolated GO flakes on a SiO_x/Si substrate. The thermal reduction decreases the 9.5 ± 1.9 Å height of the sheet by 2 to 5 Å, as obtained from the topography image (Fig. 1 and fig. S6). Two effects could lead to height reduction. One is the loss of oxygen-rich functional groups from the GO flake surface. Given that scanning an unheated tip does not result in height changes, this loss is primarily caused by intrinsic chemical conversion rather than mechanical removal. It is not possible, however, to rule out tribochemical effects at elevated temperatures. Second, the conversion of GO's sp^3 carbon bonds into sp^2 carbon bonds will flatten the material because the sp^3 carbon bonds in GO ripple the carbon skeleton, thereby increasing the sheet thickness (*22*–*24*).

Friction measurements show that variable reduction of GO could be achieved by controlling the temperature of the AFM tip. Graphene has a low friction coefficient (*25*), whereas oxides typically have higher friction coefficients. Thermal reduction should also reduce friction as the high-friction GO is replaced with lower-friction graphene. Figure 2 shows the strong correlation between the cantilever temperature during TCNL processing and the lateral force on a room-temperature tip scanned over previously reduced squares. Whereas the cantilever temperature can be precisely determined, the contact temperature must be modeled (see discussion in the SOM) (*21*); the reported temperatures are the cantilever temperatures. Reduction begins at or above 130°C, which is comparable to the results of Wu *et al.* and Mattevi *et al*., who showed that reduction starts at 100°C (*6*, *20*), presumably after the desorption of adventitious water. Higher temperatures increased the rate of reduction, as shown by the roughly linear decrease in relative friction with temperature.

Although isolated GO flakes are suited for basic studies, further technological development requires extended films of GO. Large-area GO_{epi} films (>15 mm^2) were obtained by oxidizing multilayer epitaxial graphene (EG) grown on the carbon face of SiC [see material details in the SOM (*21*)]. The oxidized films consist of multiple high-quality GO_{epi} layers that completely cover the SiC surface. AFM images show no tearing in the GO_{epi} films, indicating that they maintain their structural integrity when exposed to the harsh oxidation conditions. Figures 3 and 4 show the results obtained by performing TCNL on GO_{epi} films with different thicknesses, as determined by AFM by scratching away GO_{epi} from the SiC substrate [see the SOM (*21*)]. Figure 3 presents a zigzag rGO_{epi} nanoribbon written with a single line scan at T_{heater} ~ 1060°C on GO_{epi}. Figure 3A is an image of the current measured between a conductive platinum AFM tip and each point of the surface, showing no current on the GO surface and a current enhancement of about 100 pA in the rGO_{epi} nanoribbons. These current values are consistent with the presence of 12-nm-wide and several-nanometers-thick rGO_{epi} nanoribbons, presenting a vanishingly small Schottky barrier, and a resistive SiC substrate (resistivity of about 10^5 ohm·cm). For a 25-nm-thick GO film locally heated by a tip at 1000°C, heat flow through the layers might reduce most of the GO underneath the tip and leave only a few layers of GO at the SiC interface, as shown in the SOM (*21*). The topographical image (Fig. 3B and black graph in Fig. 3C) indicates that the reduction produces a shallow indentation of 1 nm whose origin has been previously discussed for the isolated GO sheets.

We further investigated the electrical properties of the locally reduced GO_{epi} structures using KPFM and four-point probe transport measurements in a UHV Omicron Nanoprobe system [see details in the SOM (*21*)]. The sheet resistance, R_{sheet}, of 20 μm by 20 μm squares of TCNL rGO_{epi} decreased with increasing temperature used for the TCNL local reduction, up to four orders of magnitude lower than the resistance of the original GO_{epi} (427 ± 11 megohm) (*6*). The same decrease of the in-plane resistivity was observed for extended films of rGO_{epi} produced by overnight heating of GO_{epi} in a furnace at 600°C (18 ±

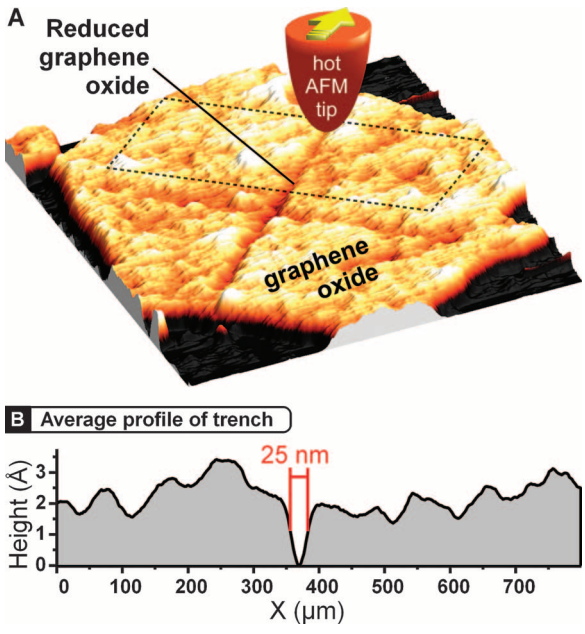

Fig. 1. Local thermal reduction of a single-layered graphene oxide flake. (**A**) Topography of a cross shape of reduced GO formed after an AFM tip heats the contact to 330°C scanned across the GO sheet at 2 μm/s. (**B**) The averaged profile of the trench outlined in (A) shows that the width (FWHM) of the line can be as narrow as 25 nm.

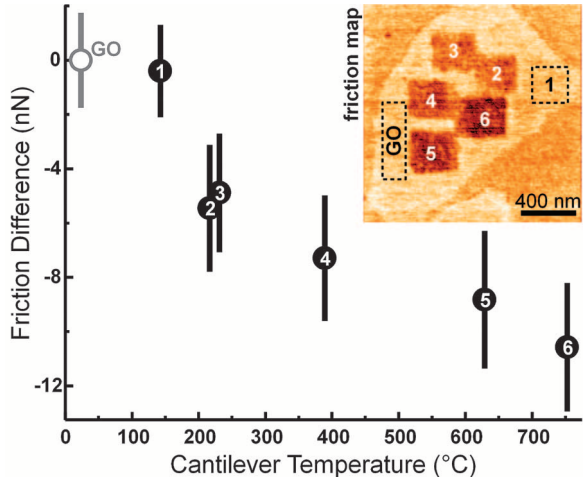

Fig. 2. The rate of thermal reduction depends on the tip temperature. The plot shows the decrease in lateral force on an AFM tip at room temperature as it scans over several squares previously reduced by TCNL at different temperatures. The inset is a room-temperature friction image of the GO sheet on which a heated tip was previously rastered twice over six square areas, at a speed of 4 μm/s. In square 1, the tip was heated during TCNL to T_{heater} ~ 100°C, yielding no apparent reduction, whereas at temperatures T_{heater} > 150°C the rastered areas (squares 2 to 6) were thermally reduced. Reduced GO, which like bulk graphite behaves as a lubricant, shows lower friction than the original GO. Higher temperatures accelerate the thermal reduction of GO and thereby more rapidly lower friction.

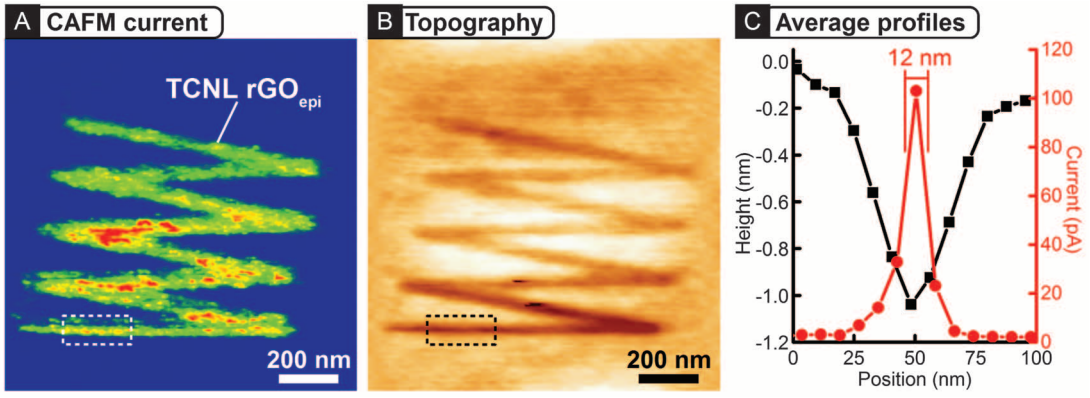

Fig. 3. Local thermal reduction of a GO_{epi} film: current and topographical images. (**A**) Room-temperature AFM current image (taken with a bias voltage of 2.5 V between tip and substrate) of a zigzag-shaped nanoribbon fabricated by TCNL on GO_{epi} at T_{heater} ~ 1060°C with a linear speed of 0.2 μm s^{-1} and a load of 120 nN. (**B**) Corresponding topography image taken simultaneously with (A). (**C**) Averaged profiles of current and height of the cross sections that are indicated as dashed lines in (A) and (B).

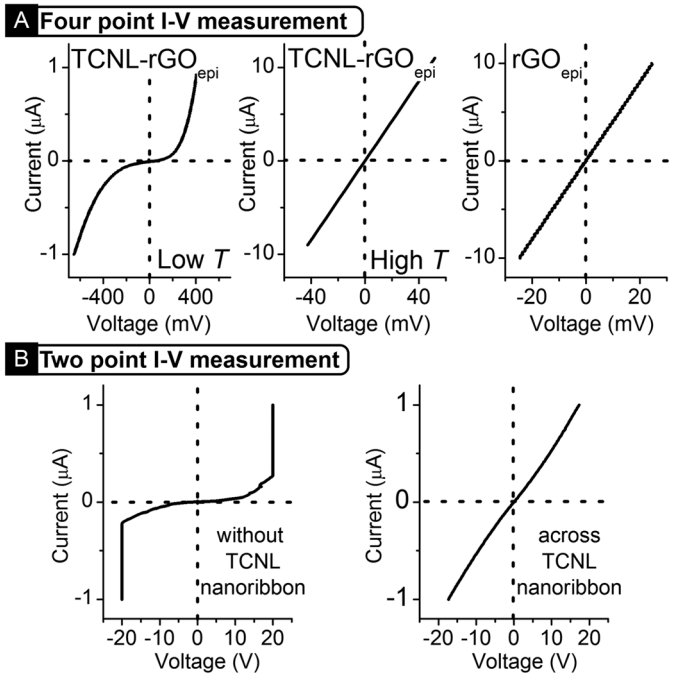

Fig. 4. Four-point and two-point transport measurements. (**A**) *I-V* curves obtained by four-point transport measurements of TCNL-reduced graphene oxide squares reduced at low temperature (Low *T*, T_{heater} ~ 600°C), TCNL-reduced graphene oxide squares reduced at high temperature (High *T*, T_{heater} ~ 1200°C), and furnace-reduced graphene oxide at 600°C in vacuum. (**B**) *I-V* curves obtained by two-point transport measurements of current between two rGO_{epi} squares with no nanoribbons in between (left curve), and between two rGO_{epi} squares with a nanoribbon in between (right curve).

10 kilohm). Furthermore, R_{sheet} and the shape of the *I-V* characteristics could be varied by changing the temperature of the AFM probe (in Fig. 4A, R_{sheet} = 9174 kilohm and 30 kilohm for low and high temperature, respectively). Kelvin probe measurements show that TCNL rGO_{epi} displays a contact potential change of 168 ± 54 mV in respect to GO_{epi}, similar to that of bulk reduced rGO (188 ± 96 mV). The presence of residual oxygen and structural disorder led to the large difference in conductivity between epitaxial graphene and rGO_{epi} or TCNL-rGO_{epi}.

We also analyzed an isolated TCNL-rGO_{epi} nanoribbon (Fig. 4B) with a length of 25 μm and a width of 100 nm, as measured by AFM. We acquired *I-V* data by placing conductive tips on top of two micrometer-sized squares of rGO_{epi} fabricated in situ by an electron beam at each end of the nanoribbon. Two-point transport measurements indicated a resistance larger than 2 gigohm when the tips were placed at an arbitrary position on the GO surface (very large barrier at the contact) and a drop in resistance from 120 megohm (between the two squares with no nanoribbon) to 20 megohm (between the two squares connected by the nanoribbon). The transport changed from insulating to metallic (i.e., linear *I-V* curves) in the presence of the TCNL-rGO_{epi} nanoribbon between the squares (Fig. 4B). By using the relation $R_{sheet} = (R_{ribbon} \cdot w \cdot t_{ribbon})/(L \cdot t_{sheet})$ (*26*) and assuming a 13-nm-thick nanoribbon, we obtain a sheet resistance of 65 kilohm, in good agreement with the measurements reported in Fig. 4A for microscopic squares of TCNL-rGO_{epi}.

TCNL does not require any solvents or lithographic resists that could contaminate the sample. This is especially important because the electronic properties of graphene vary strongly with surface doping. The strategy of variably reducing extended GO films is a general one that could be implemented in multiple ways depending on the application. The manufacture of graphene nanoelectronics could be achieved by using arrays of heated probe tips (*18*). Independently addressed heated probe tips could alternately read or write nanostructures on a surface and in large arrays could address wafer-scale areas at high speed. A nano-embossing approach might also achieve local GO reduction, provided that the imprint template would offer nanometer-scale control of the reducing temperature field.

References and Notes

1. C. Berger *et al.*, *Science* **312**, 1191 (2006).
2. J. Kedzierski *et al.*, *IEEE Trans. Electron. Dev.* **55**, 2078 (2008).
3. D. A. Dikin *et al.*, *Nature* **448**, 457 (2007).
4. S. Park, R. S. Ruoff, *Nat. Nanotechnol.* **4**, 217 (2009).
5. G. Eda, C. Mattevi, H. Yamaguchi, H. Kim, M. Chhowalla, *J. Phys. Chem. C* **113**, 15768 (2009).
6. X. S. Wu *et al.*, *Phys. Rev. Lett.* **101**, 026801 (2008).
7. A. J. Epstein, in *Conductive Polymers and Plastics: In Industrial Applications*, L. Rupprecht, Ed. (William Andrew, Norwich, NY, 1999), pp. 1–4.
8. C. E. Parman, N. E. Israeloff, J. Kakalios, *Phys. Rev. B* **47**, 12578 (1993).
9. J. T. Robinson, F. K. Perkins, E. S. Snow, Z. Q. Wei, P. E. Sheehan, *Nano Lett.* **8**, 3137 (2008).
10. J. T. Robinson *et al.*, *Nano Lett.* **8**, 3441 (2008).
11. D. Wang *et al.*, *Appl. Phys. Lett.* **95**, 233108 (2009).
12. D. Wang *et al.*, *Adv. Funct. Mater.* **19**, 3696 (2009).
13. R. Szoszkiewicz *et al.*, *Nano Lett.* **7**, 1064 (2007).
14. D. Wang *et al.*, *Appl. Phys. Lett.* **91**, 243104 (2007).
15. P. E. Sheehan, L. J. Whitman, W. P. King, B. A. Nelson, *Appl. Phys. Lett.* **85**, 1589 (2004).
16. M. Yang, P. E. Sheehan, W. P. King, L. J. Whitman, *J. Am. Chem. Soc.* **128**, 6774 (2006).
17. B. A. Nelson, W. P. King, A. R. Laracuente, P. E. Sheehan, L. J. Whitman, *Appl. Phys. Lett.* **88**, 033104 (2006).
18. P. Vettiger *et al.*, *IEEE Trans. NanoTechnol.* **1**, 39 (2002).
19. C. Gómez-Navarro *et al.*, *Nano Lett.* **7**, 3499 (2007).
20. C. Mattevi *et al.*, *Adv. Funct. Mater.* **19**, 2577 (2009).
21. See supporting material available on *Science* Online.
22. G. Eda, G. Fanchini, M. Chhowalla, *Nat. Nanotechnol.* **3**, 270 (2008).
23. H. C. Schniepp *et al.*, *J. Phys. Chem. B* **110**, 8535 (2006).
24. J. C. Meyer *et al.*, *Nature* **446**, 60 (2007).
25. T. Filleter *et al.*, *Phys. Rev. Lett.* **102**, 086102 (2009).
26. The thickness of the ribbon, t_{ribbon}, and the thickness of the sheet, t_{sheet}, have been inferred from the thickness of the corresponding GO films as reported in the SOM.

27. This work has been supported by the National Science Foundation (CMDITR program DMR 0120967, Materials Research Science and Engineering Center program DMR

0820382, and DMR-0706031), U.S. Department of Energy (DE-FG02-06ER46293 and PECASE), the Institute for Nanoscience at Naval Research Laboratory (NRL), the Office of Naval Research of the United States, the Defense Advanced Research Projects Agency (DARPA) Tip-Based Nanomanufacturing program, and Georgia Institute of Technology (Georgia Tech Research Foundation, COE Cutting Edge Research Award, and COPE fellowship). This research was performed while Z.W. held a National Research Council Research Associateship Award at Naval Research Laboratory of the United States. Z.W. thanks H. Qi at NRL for providing doped silicon wafers, evaporating gold layers on mica, and taking scanning electron micrograph images of GO sheets on gold and silicon substrates. E.R. thanks T.-D. Li and M. Lucas for support with CAFM.

Supporting Online Material
www.sciencemag.org/cgi/content/full/328/5984/1373/DC1
Materials and Methods
Figs. S1 to S8
References and Notes

9 February 2010; accepted 29 April 2010
10.1126/science.1188119

Quaternary Ammonium (Hypo)iodite Catalysis for Enantioselective Oxidative Cycloetherification

Muhammet Uyanik,[1] Hiroaki Okamoto,[1] Takeshi Yasui,[1] Kazuaki Ishihara[1,2]*

It is desirable to minimize the use of rare or toxic metals for oxidative reactions in the synthesis of pharmaceutical products. Hypervalent iodine compounds are environmentally benign alternatives, but their catalytic use, particularly for asymmetric transformations, has been quite limited. We report here an enantioselective oxidative cycloetherification of ketophenols to 2-acyl-2,3-dihydrobenzofuran derivatives, catalyzed by in situ–generated chiral quaternary ammonium (hypo)iodite salts, with hydrogen peroxide as an environmentally benign oxidant. The optically active 2-acyl 2,3-dihydrobenzofuran skeleton is a key structure in several biologically active compounds.

Over the past two decades, hypervalent iodine compounds have been increasingly explored as environmentally benign oxidation reagents in place of rare or toxic heavy metal oxidants (*1*, *2*). However, their stoichiometric use has been limited because of potentially explosive shock-sensitivity and/or poor solubility in common organic solvents (*1*, *2*). Thus, the development of hypervalent iodine-catalyzed reactions using more convenient stoichiometric co-oxidants is needed (*3*, *4*). Harnessing chiral hypervalent iodine compounds for enantioselective oxidative coupling has proven a particular challenge in asymmetric catalysis. There are several examples of catalysis by in situ–generated chiral aryl-λ^3- or aryl-λ^5-iodane (*5*) with *meta*-chloroperbenzoic acid (*m*-CPBA) as a co-oxidant (Fig. 1A, left) (*6*–*9*); these include Quideau *et al.*'s enantioselective hydroxylative dearomatization of phenols (*6*), Altermann *et al.*'s enantioselective α-oxysulfonylation of ketones (*7*), and Dohi *et al.*'s and our independently reported enantioselective oxidative spirolactonizations of 1-napthol derivatives (*8*, *9*). In contrast, no strong examples have emerged of asymmetric catalysis using chiral cations paired with inorganic iodine-derived oxoacids, such as hypoiodous acid [IOH, I(I)], iodous acid [O=IOH, I(III)], iodic acid [$(O=)_2$IOH, I(V)], and periodic acid [$(O=)_3$IOH, I(VII)].

We report here an implementation of this strategy, using the atom-economical hydrogen peroxide as a mild stoichiometric oxidant to activate catalytic ion pairs of chiral quaternary ammonium iodide (Fig. 1A, right) (*10*, *11*). Specifically, we targeted enantioselective oxidative cycloetherification of ketophenols to 2-acyl-2,3-dihydrobenzofuran derivatives, using a C_2-symmetric chiral binaphthyl-based quaternary ammonium (hypo)iodite catalyst generated in situ by reaction with hydrogen peroxide (Fig. 1B). The chiral 2-substituted 2,3-dihydrobenzofuran skeleton is a key structure in several biologically active compounds of medicinal interest (*12*–*19*). Earlier preparations of optically active 2-alkenyl-2,3-dihydrobenzofuran derivatives have relied on transition metal catalysis (*20*–*23*).

The catalytic or stoichiometric oxidation of 3-(2-hydroxyphenyl)-1-phenylpropan-1-one (**1**) with phenyl-λ^3-iodanes gave a complex mixture, and the desired (2,3-dihydrobenzofuran-2-yl)(phenyl)methanone (**2**) was not detected (Fig. 2A, entries 1 and 2). In sharp contrast, and to our delight, the oxidation of **1** with two equivalents of hydrogen peroxide [30 weight percent (wt %) in water] in the presence of 10 mole percent (mol %) of tetrabutylammonium iodide (Bu_4NI) in acetonitrile at room temperature gave **2** in 87% yield (Fig. 2A, entry 3) (*24*). Furthermore, the oxidation of **1** was much faster in diethyl ether (Et_2O), tetrahydrofuran (THF), or ethyl acetate (EtOAc) (Fig. 2A, entry 4, and table S1). Notably, the oxidation of **1** did not occur on substitution of tetrabutylammonium bromide or chloride for Bu_4NI. Excellent chemoselectivity was observed

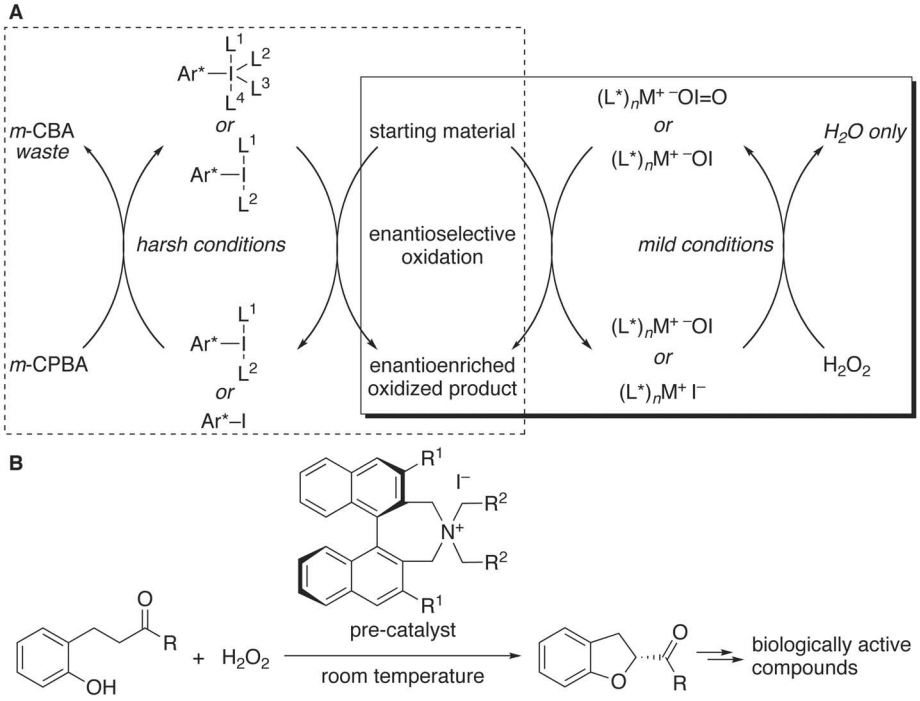

Fig. 1. (**A**) (Left) Known in situ–generated aryl-λ^3- or aryl-λ^5-iodane catalysis. (Right) In situ–generated hypoiodite(I) or iodite(III) catalysis. (**B**) Design of inorganic iodide precatalyst paired with a chiral quaternary ammonium counter ion for the enantioselective oxidative cycloetherification of ketophenols to 2-acyl-2,3-dihydrobenzofuran derivatives. Ar, aryl; L, ligand; M^+, metal or onium cation, R, alkyl or aryl group. Symbols (Ar and L) marked with asterisks represent chiral groups.

[1]Graduate School of Engineering, Nagoya University, Furo-cho, Chikusa, Nagoya, 464-8603, Japan. [2]Core Research for Evolutional Science and Technology, Japan Science and Technology Agency, Furo-cho, Chickusa, Nagoya, 463-8603, Japan.

*To whom correspondence should be addressed. E-mail: ishihara@cc.nagoya-u.ac.jp